A Model Study of Zonal Forcing in the Equatorial Stratosphere by Convectively Induced Gravity Waves

M. J. ALEXANDER AND J. R. HOLTON

Department of Atmospheric Sciences, University of Washington, Seattle, Washington

(Manuscript received 16 April 1996, in final form 16 July 1996)

ABSTRACT

A two-dimensional cloud-resolving model is used to examine the possible role of gravity waves generated by a simulated tropical squall line in forcing the quasi-biennial oscillation (QBO) of the zonal winds in the equatorial stratosphere. A simulation with constant background stratospheric winds is compared to simulations with background winds characteristic of the westerly and easterly QBO phases, respectively. In all three cases a broad spectrum of both eastward and westward propagating gravity waves is excited. In the constant background wind case the vertical momentum flux is nearly constant with height in the stratosphere, after correction for waves leaving the model domain. In the easterly and westerly shear cases, however, westward and eastward propagating waves, respectively, are strongly damped as they approach their critical levels, owing to the strongly scale-dependent vertical diffusion in the model. The profiles of zonal forcing induced by this wave damping are similar to profiles given by critical level absorption, but displaced slightly downward. The magnitude of the zonal forcing is of order 5 m s^{-1} day^{-1}. It is estimated that if 2% of the area of the Tropics were occupied by storms of similar magnitude, mesoscale gravity waves could provide nearly 1/4 of the zonal forcing required for the QBO.

1. Introduction

In their theory of the quasi-biennial oscillation (QBO) of the zonal mean winds in the equatorial stratosphere, Lindzen and Holton (1968, hereafter LH68) argued that zonal forcing induced by a continuous spectrum of long-period vertically propagating gravity waves was responsible for the downward propagating easterly and westerly mean wind regimes that characterize the QBO. In LH68 the wave-induced forcing of the mean flow was attributed to absorption of these vertically propagating waves at ''critical levels'' where their Doppler-shifted horizontal phase speeds vanish. According to this hypothesis, waves with a broad spectrum of zonal phase speeds would be absorbed in a shear zone in which the mean zonal wind speeds match the phase speeds of the waves. LH68 showed that if the gravity wave spectrum contained components with both positive and negative zonal phase speeds, the critical level absorption mechanism could lead to a mean zonal flow oscillation with alternating downward propagating westerly and easterly shear zones, provided that a mechanism existed to initiate the shear zones in the upper stratosphere. In LH68 this initiation mechanism was taken to be the observed semiannual oscillation centered near the equatorial stratopause.

Somewhat later, and motivated by observational studies of large-scale equatorial waves (Maruyama 1969; Wallace and Kousky 1968), Holton and Lindzen (1972, hereafter HL72) offered an alternative to the LH68 model in which the zonal forcing was attributed to two large-scale monochromatic equatorial wave modes, an eastward propagating Kelvin wave, and a westward propagating Rossby–gravity wave. In HL72 the wave-induced forcing of the mean flow was attributed to radiative damping of the long-period Kelvin and Rossby–gravity waves rather than to critical level absorption. Since the rate of radiative damping increases rapidly as the Doppler-shifted phase speed decreases, Kelvin waves will be preferentially damped and produce eastward accelerations in westerly shear zones, while Rossby–gravity waves will be preferentially damped and produce westward accelerations in easterly shear zones. Because waves are damped below their critical levels, this mechanism no longer requires a separate process to initiate shear zones at high levels (Plumb 1977).

The HL72 model was able to produce an oscillation similar in character to that of the LH68 model. However, it was soon recognized by Lindzen and Tsay (1975) that an additional equatorial easterly gravity wave mode was required to account for the observed easterly acceleration of the QBO. More recently, Dunkerton (1991) showed that when vertical advection by the mean up-

Corresponding author address: Dr. James R. Holton, Dept. of Atmospheric Sciences, University of Washington, Box 351640, Seattle, WA 98195-1640.
E-mail: holton@atmos.washington.edu

welling in the equatorial stratosphere is taken into account, observed Kelvin and Rossby–gravity wave fluxes are much too small to generate the observed QBO. Studies by Gray and Pyle (1989) with a two-dimensional model and Takahashi and Boville (1992) with a three-dimensional model confirmed that in the presence of mean upwelling the Kelvin and Rossby–gravity wave fluxes must be at least a factor of 2 greater than are observed in order to produce a realistic QBO.

Recently, Dunkerton (1996) considered the QBO momentum problem in some detail. He showed that if a suitable spectrum of mesoscale gravity waves is added to the observed Kelvin and Rossby–gravity waves, the combined zonal forcing can produce a realistic QBO (including the observed asymmetries between the easterly and westerly shear zones) even in the presence of mean upwelling. Dunkerton used the gravity wave momentum flux parameterization of LH68, and a Kelvin and Rossby–gravity wave damping parameterization similar to that used in HL72 (Lindzen 1971). Thus, it now appears that a combination of the models of LH68 and HL72 is required to explain the observed QBO.

Although LH68 emphasized the likely importance of equatorially trapped internal gravity waves of large horizontal and small vertical scale, their parameterization for the wave-induced force was actually derived from consideration of internal gravity waves in the absence of rotation and, thus, was more applicable to mesoscale gravity waves. At the time of the writing of LH68 there was little direct observational evidence of such gravity waves in the equatorial atmosphere. However, in recent years analysis of high-resolution radiosonde data (e. g., Sato et al. 1994; Tsuda et al. 1994; Allen and Vincent 1995; Karoly et al. 1996), data from high-altitude research aircraft flights (Alexander and Pfister 1995; Pfister et al. 1993), and satellite cloud images (Bergman and Salby 1994) all suggest a substantial role for convectively generated mesoscale gravity waves in the equatorial region.

The morphology of gravity waves generated by specific equatorial convective systems is, however, still unclear. Little is known about the spectral distribution of waves generated by tropical convection, their propagation into the stratosphere, and their interaction with the mean flow. In this work we employ a two-dimensional numerical model of a tropical squall line. Although convective systems often show a tendency to occur in lines or bands, the squall line is a less general case, chosen because its symmetry makes a two-dimensional modeling approach reasonable and because the tropospheric properties of such systems have been studied in detail elsewhere (e. g., Houze 1993).

The object of the present study is to examine the gravity wave fluxes in the stratosphere simulated by this special type of tropical convection and to show that the vertically propagating gravity waves generated by such a system may play a significant role in the momentum budget of the lower equatorial stratosphere.

2. Numerical model

The tropical squall line simulations were carried out with the nonhydrostatic cloud resolving model of Durran and Klemp (1983), who provided details of the cloud microphysical parameterizations and the numerical solution method used in the model. The same model was previously used by Fovell et al. (1992) and Alexander et al. (1995) to study gravity waves produced by a simulated two-dimensional midlatitude squall line.

The version of the model used here is only slightly altered from that used by Alexander et al. (1995). The model domain is 900 km wide and 30 km deep. Grid spacings are 1.5 km in the horizontal and 0.25 km in the vertical. The high resolution in the vertical is designed to resolve the shallow cold pool near the surface and to resolve short vertical wavelength gravity waves in the stratosphere. The radiation boundary condition of Durran (1995) is used at the upper boundary. In addition, to avoid spurious cooling near the upper boundary, it is necessary to include a ''sponge'' layer in which the potential temperature is relaxed toward the initial profile by Newtonian cooling at a rate increasing uniformly from zero at the 27-km level to a maximum of 5.0×10^{-5} s^{-1} at the top boundary. A radiation boundary condition is also employed at the lateral boundaries. But, to prevent noise from developing near these boundaries in the troposphere, it is also necessary to include a second-order smoothing operator, which is applied to all fields at grid points within 30 km of both lateral boundaries.

To prevent nonlinear instability, weak fourth-order diffusion is applied to all prognostic fields in the horizontal and to the velocity and pressure fields in the vertical. The fourth-order vertical smoothing has an *e*-folding decay time of about 400 s for a vertical wavelength of 1 km, 6300 s for a vertical wavelength of 2 km, and has a negligible effect for waves of vertical wavelength greater than 4 km. Because the vertical wavelength shrinks rapidly as a wave approaches its critical level, the fourth-order vertical smoothing has important implications for damping of waves in shear zones in the simulations reported here.

In addition to the fourth-order smoothing required to prevent nonlinear instability, there is also a parameterized, Richardson-number-dependent, subgrid-scale mixing in the model as described in Durran and Klemp (1983). For the cases reported here, subgrid-scale mixing is only important in the troposphere. The fourth-order numerical diffusion generally damps waves in the stratosphere before the Richardson number becomes sufficiently small to activate the explicit subgrid-scale mixing parameterization.

The initial thermodynamic and tropospheric wind soundings (Fig. 1) are specified to approximately simulate conditions of the West African squall lines studied by Redelsperger and Lafore (1988) and Lafore and Moncrieff (1989). The specified thermodynamic sounding has an unusually high conditional instability for the

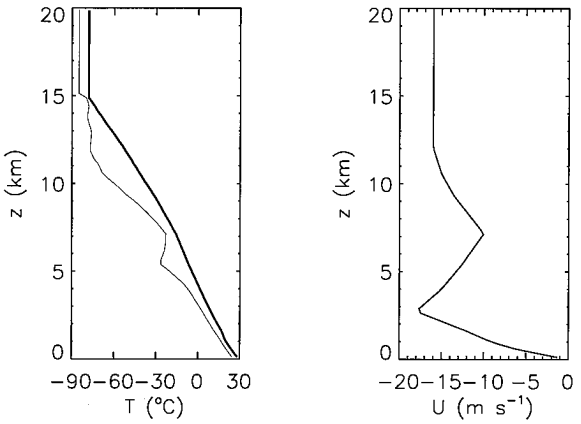

FIG. 1. Initial thermodynamic and wind soundings used in the tropical squall line simulations. The left panel shows temperature (thick) and dewpoint temperature (thin). The right panel shows the tropospheric wind profile used in all simulations. The winds are a constant -16 m s^{-1} above the tropopause in the control simulation. Stratospheric shear cases are shown in Fig. 2.

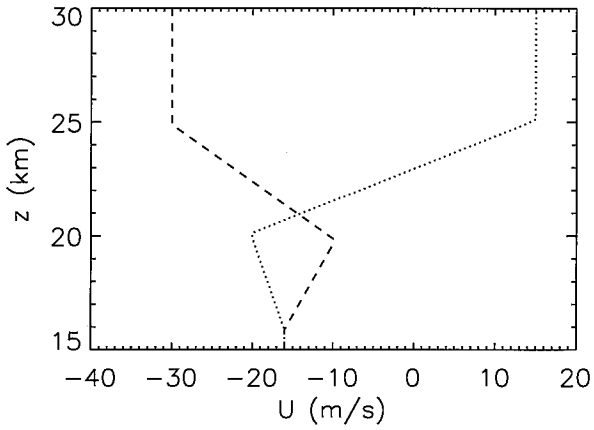

FIG. 2. Stratospheric wind profiles for simulations of the easterly (dashed line) and westerly (dotted line) phases of the QBO.

Tropics. Simulations with varying thermodynamics soundings (not shown) demonstrate that for the two-dimensional version of the cloud model used here, rather large values of conditional instability are required for development of sustained mesoscale convection.

In order to analyze the possible contribution of gravity waves generated by squall lines to acceleration of mean winds in the QBO, three simulations are compared. In the first case (labeled the ''control''), winds above the tropopause are constant with height at -16 m s^{-1}. The model domain also translates at a constant speed of -16 m s^{-1}. Thus, stratospheric waves are viewed in an intrinsic frame of reference (i.e., phase speeds relative to the model domain are the Doppler-shifted phase speeds in the stratosphere). Since the speed of motion of the squall line is only about -5 m s^{-1} in the translating domain, the squall line remains well within the domain throughout a 12-h simulation period. The other two cases (labeled the ''easterly shear'' and ''westerly shear'' cases, respectively) have the wind profiles above the tropopause used by Holton (1972) to represent the easterly and westerly phases of the QBO, respectively (Fig. 2).

The simulations for each of the three cases were run for 12 h, and field variables were saved at 3-min intervals for the last 8 h of each simulation. The overall structure of the control case at 6 h is shown in Fig. 3, which may be compared with Fig. 2 of Alexander et al. (1995). Temporal variability in the strength of the squall line is illustrated in Fig. 4, which shows a longitude–time cross section of rainfall rate. It is clear from Fig. 4 that the squall line drifts slowly westward in the model domain. But the average speed of drift is only -4.9 m s^{-1} in the moving frame, so that the convection remains far from the boundaries throughout the integration period. Figure 4, which may be compared with Fig. 3 of Fovell et al. (1992), indicates that the variability in these tropical simulations is less regular than the quasiperiodic variability seen in the midlatitude cases previously simulated. Thus a longer period was deemed necessary for diagnosis of the wave spectra.

3. Wave momentum fluxes

The properties of gravity waves produced in the simulations can be conveniently characterized using the two-dimensional (x, t) spectral analysis approach described in detail in Alexander et al. (1995). This analysis is carried out for the period 4 h $\leq t \leq$ 11 h. Because average travel times for gravity wave energy across the vertical stratospheric domain are 2–3 h, this analysis period excludes start-up artifacts. Also, transience will be effectively averaged out and will not artificially appear as vertical variations in the momentum flux. Only grid points in the range 0 km $\leq x \leq$ 768 km are included in the spectral analysis in order to give approximately equal weighting to the regions upstream and downstream of the squall line gust front.

Spectra of vertical velocity and of momentum flux show similar features as those discussed in Alexander et al. (1995) for a midlatitude case. In that previous work, spectral power was concentrated along a line of constant vertical wavelength of 8 km, corresponding to the depth of the convective heating in the troposphere. In this tropical case, there is more variability in the depth of convective heating as a function of time. The spectrum of stratospheric gravity waves correspondingly shows power scattered more broadly between vertical wavelengths of 2–15 km—the upper limit of this range associated with the depth of the troposphere. Two pronounced peaks at 5 and 6 km correspond to the heating associated with the rearward propagating cells, which have 5–6 km depth in this simulation. Unlike the midlatitude case, no pronounced peaks appear in the frequency spectrum, suggesting a less important role for the ''mechanical pumping'' mechanism of wave gen-

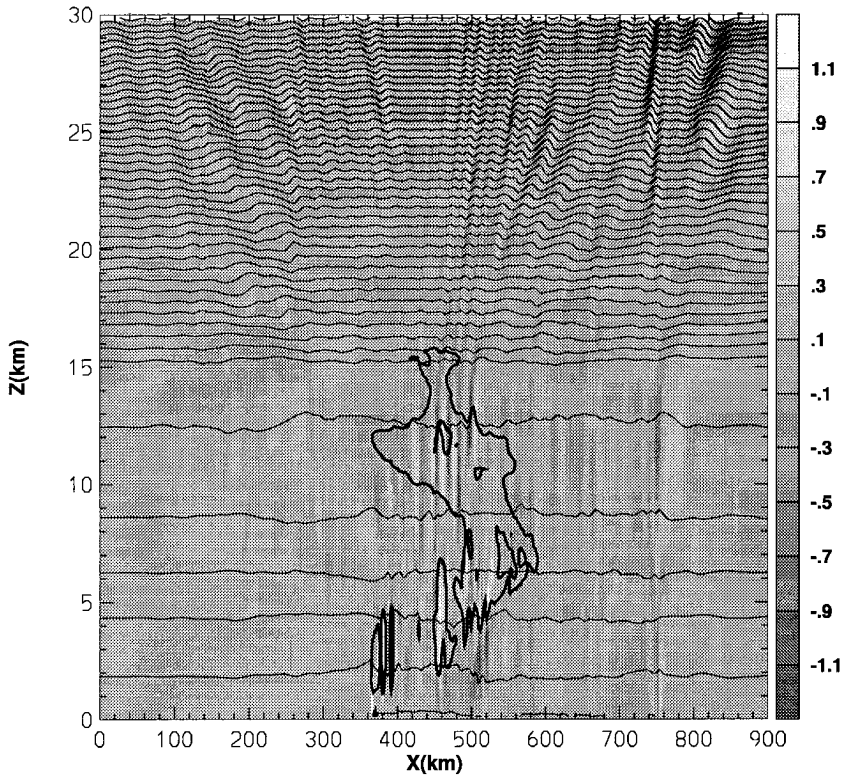

FIG. 3. The control simulation at 6 h of simulation time. Shading represents contours of vertical velocity. (Contrast has been enhanced to show the qualitative structure; the full range of vertical velocities is ± 5 m s^{-1}.) Thin lines are isentropes (at 10-K intervals), and the thick line shows the cloud outline (cloud water fraction = 10^{-4} g g^{-1}). The surface gust front appears at ~370 km.

eration (Fovell et al. 1992) in this tropical case, perhaps due to the shallower penetration of the convection relative to the higher tropical tropopause.

As in the midlatitude simulations, the control case (Fig. 3) has waves propagating both ahead of and to the rear of the westward moving squall line, but there is a clear dominance of rearward traveling gravity waves. The dominance of rearward propagating waves has recently been confirmed in observations of inertia–gravity waves from tropical Australia (Hamilton and Vincent 1995). The easterly and westerly QBO phase cases (Fig. 5) show dramatic evidence of wave absorption in shear zones and of ray path curvature owing to Doppler shifting of wave frequencies by mean flow shear.

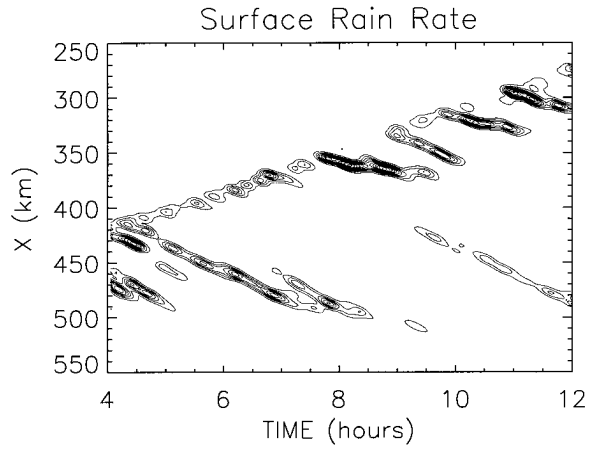

FIG. 4. Contours of surface rainfall vs time and longitude *(x)* for the control simulation. The contour interval is 10^{-4} g g^{-1} (rainwater fraction). Intense rainfall is associated with the leading edge of the line (which moves westward) and rearward propagating cells (eastward).

The damping of waves as they approach their critical levels has a profound influence on the wave spectra. Figure 6 shows the zonal phase speed spectra of momentum flux for the westerly QBO case at several levels between 15 and 25 km. These spectra represent time averages over the 7-h analysis window. Near the tropopause there is a broad distribution of waves in the phase speed range of $\sim \pm 30$ m s^{-1}. As height increases, there is an overall decrease in amplitude owing to propagation of waves out of the domain through the side boundaries. But between 20 and 24 km, in the strong westerly shear zone, there is a rapid filtering of the positive phase speed waves as waves of increasing phase speed encounter their critical levels.

The effects of this filtering are clearly shown in the

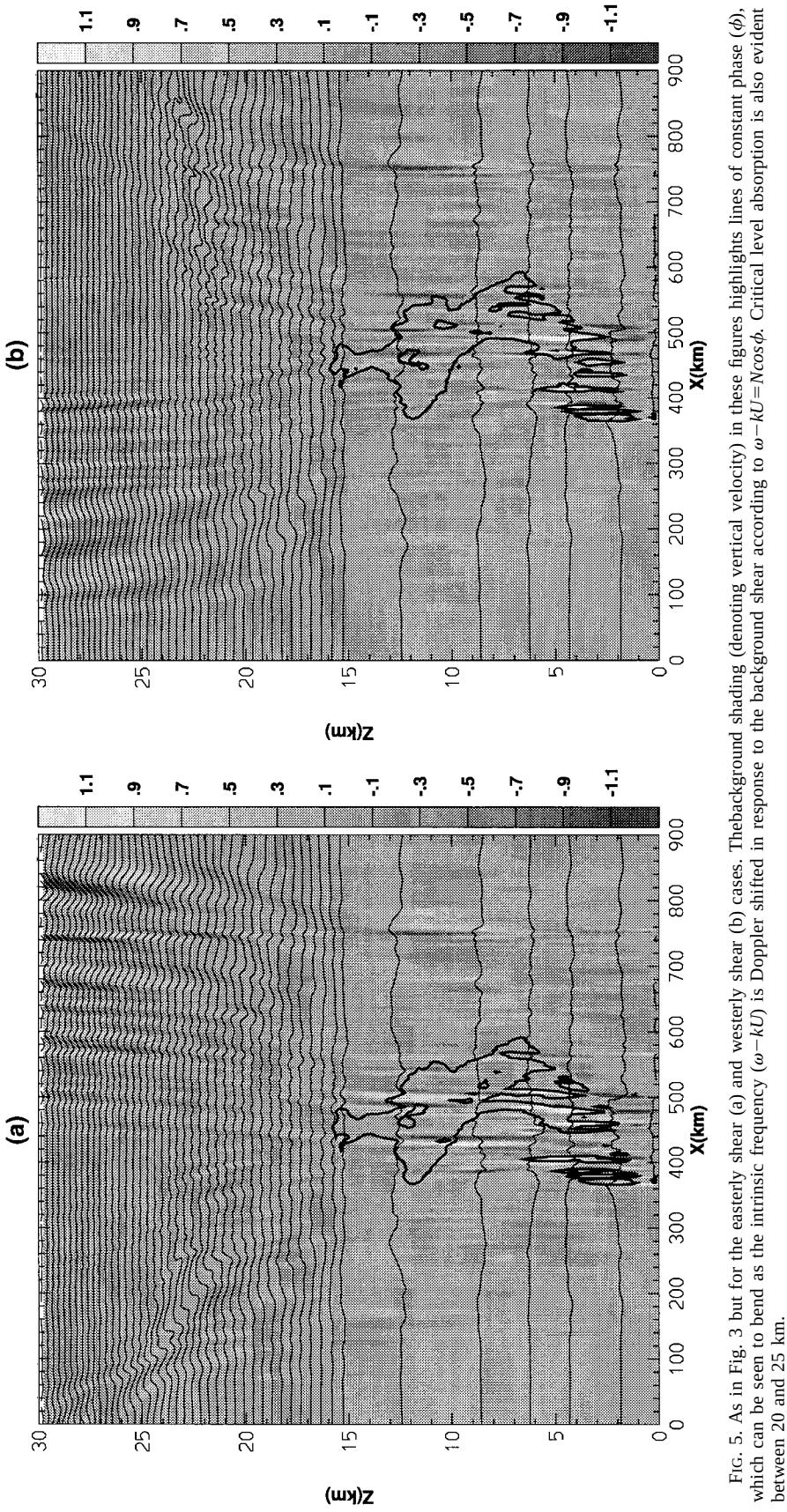

FIG. 5. As in Fig. 3 but for the easterly shear (a) and westerly shear (b) cases. Thebackground shading (denoting vertical velocity) in these figures highlights lines of constant phase (ϕ), which can be seen to bend as the intrinsic frequency ($\omega - kU$) is Doppler shifted in response to the background shear according to $\omega - kU = N\cos\phi$. Critical level absorption is also evident between 20 and 25 km.

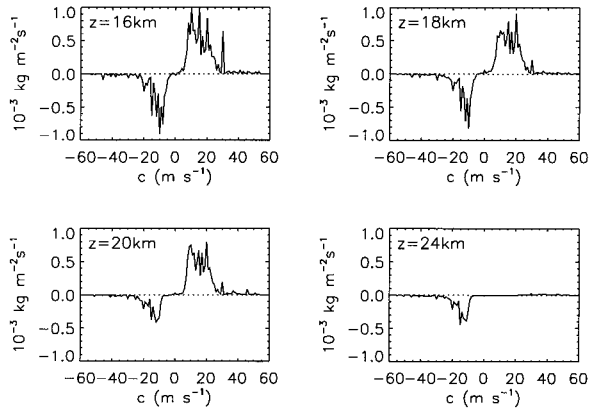

FIG. 6. Spectra of momentum flux vs phase speed c in the -16 m s^{-1} moving frame. This is the intrinsic frame of reference at the tropopause. Spectra at $z = 16$, 18, 20, and 24 km are shown for the westerly shear case. Fluxes are computed as density times the cospectrum of u' and w' per unit phase speed. These spectra would be constant in height for linear, conservative waves in a closed domain, so changes reflect dissipation and cross-boundary fluxes.

zonal- and time-averaged vertical profiles of eastward and westward momentum fluxes shown in Fig. 7. In the control case, the eastward momentum flux dominates over westward flux, and both the eastward and westward momentum fluxes decrease with height fairly uniformly. As will be shown in the next section, below the sponge layer this decrease with height is accounted for by waves leaving the domain at the lateral boundaries. In the easterly QBO phase case the eastward momentum decreases substantially in the 15–20 km layer owing to the westerly shear associated with the westerly wind peak at 20 km. But between 21 and 24 km there is a very rapid decrease of westward momentum fluxes, corresponding to filtering by the main easterly shear zone. The situation is basically reversed in the westerly QBO phase case. In this case the westward momentum fluxes decrease substantially in the weak easterly shear zone below 20 km, and the eastward propagating waves are nearly all removed between 20 and 23 km in the main westerly shear zone.

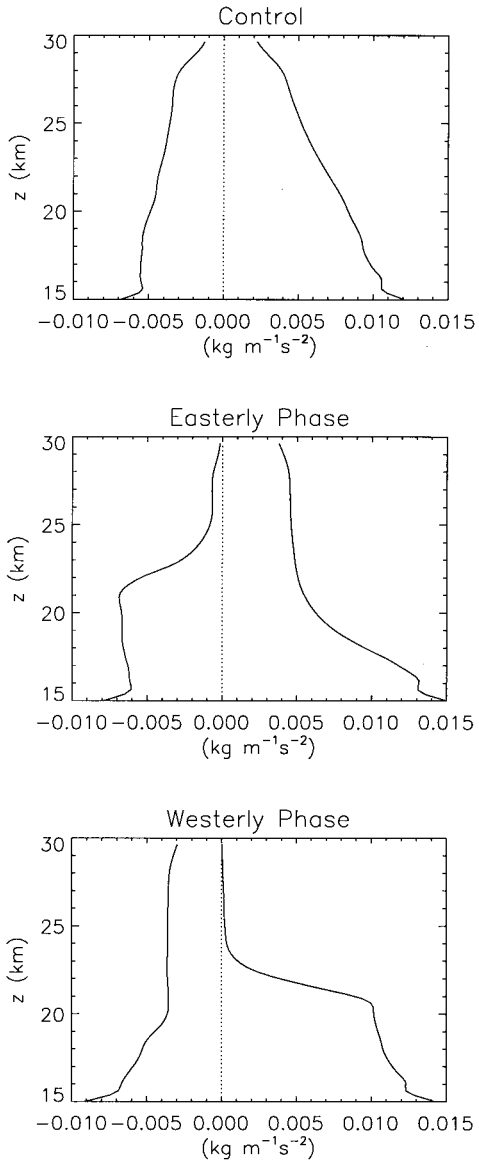

FIG. 7. Three panels showing separate profiles of eastward and westward gravity wave momentum flux averaged over the *(x,t)* domain for the control (top), easterly QBO (middle), and westerly QBO (bottom) cases.

4. Mean flow forcing

The mean-flow forcing cannot be estimated simply by evaluating the net momentum flux convergence in the model domain because, as is clear from Figs. 3 and 5, westward and eastward propagating waves both propagate horizontally out of the domain. The vertical momentum fluxes computed over the model domain shown in Fig. 7 must be corrected for this effect. Such a correction can be carried out using the wave activity conservation principle.

The method can be illustrated by considering a monochromatic wave of phase $\phi = kx + mz - \omega t$, where k and m are the zonal and vertical wavenumbers, and ω is the frequency. Then for a slowly varying basic state, wave activity conservation for steady (i.e., time averaged) conservative waves can be expressed approximately as (Andrews et al. 1987)

$$\frac{\partial \langle c_{gx} A \rangle}{\partial x} + \frac{\partial \langle c_{gz} A \rangle}{\partial z} = 0, \tag{1}$$

where angle brackets denote a time average, $A \equiv kE/(\omega - kU)$ is the ''wave activity''(sometimes referred to as pseudomomentum), and the wave energy E is defined by

$$E \equiv \rho_s \left[\frac{\overline{u'^2}}{2} + \frac{\overline{w'^2}}{2} + \frac{\overline{(g\theta'/\theta_s)^2}}{2N^2} \right]. \tag{2}$$

In (2), u', w', and θ' denote the disturbance zonal velocity, vertical velocity, and potential temperature, respectively; overbars denote averages over a wave cycle; $\rho_s(z)$ and $\theta_s(z)$ denote basic state density and potential temperature, respectively; and N is the buoyancy frequency. Since, as shown below, $c_{gz}A$ is equivalent to the vertical momentum flux, (1) can be used to estimate the momentum flux convergence associated with wave activity leaving the domain horizontally.

Equation (1) can be expressed in a convenient form for numerical evaluation by using the relationships among the wave fields obtained from linear wave theory. If wave solutions are specified of the form

$$(u',\ w',\ \theta') = \mathrm{Re}[(\hat{u},\ \hat{w},\ \hat{\theta})\ \exp(i\phi)], \tag{3}$$

where $\hat{u}$, $\hat{w}$, and $\hat{\theta}$ denote the amplitudes of the perturbations, then it can easily be shown (e.g., Holton 1992) that

$$\hat{u} = -(m/k)\hat{w} \tag{4}$$

and

$$(g\hat{\theta}/\theta_s) = -[iN^2/(\omega - kU)]\hat{w}, \tag{5}$$

where k, m, and ω are related by the dispersion equation

$$(\omega - kU)^2/N^2 = k^2/(k^2 + m^2). \tag{6}$$

The zonal and vertical components of the group velocity are thus

$$(c_{gx},\ c_{gz}) \equiv \left(\frac{\partial\omega}{\partial k},\ \frac{\partial\omega}{\partial m}\right) = \frac{(m,\ -k)Nm}{(k^2 + m^2)^{3/2}}. \tag{7}$$

From (4)–(6) the wave energy of (2) can be expressed as

$$E = \rho_s\frac{\hat{u}^2}{2}\left(\frac{k^2 + m^2}{m^2}\right), \tag{8}$$

and using the definition of A the vertical momentum flux can then be expressed as

$$\rho_s\overline{u'w'} = -\rho_s\frac{k}{m}\left(\frac{\hat{u}^2}{2}\right) = c_{gz}A. \tag{9}$$

Similarly, it can be shown that

$$c_{gx}A = \left(\frac{m^2}{k^2 + m^2}\right)E = \rho_s\left(\frac{\hat{u}^2}{2}\right). \tag{10}$$

Substituting from (9) and (10) into (1) and integrating over the horizontal domain $0 \le x \le L_x$ then yields the desired result

$$-\frac{1}{\rho_s}\frac{\partial}{\partial z}\langle\rho_s\overline{u'w'}\rangle = -L_x^{-1}\left[\left|\frac{\langle\hat{u}^2\rangle}{2}\right|_{x=0} - \left|\frac{\langle\hat{u}^2\rangle}{2}\right|_{x=L_x}\right]. \tag{11}$$

Thus the convergence of momentum flux owing to wave activity propagating sideways out of the domain can be easily measured as the difference in the zonal kinetic energy of the waves at the left and right boundaries of the domain.

Although (11) has been derived for a monochromatic wave, it is simple to extend the result to a spectrum of waves simply by summing the amplitudes on the right-hand side over all the spectral components. Figure 8 shows the result of such a calculation for the control case. The boundary effect produces an apparent eastward forcing in the domain in this case. This is consistent with the fact that eastward propagating waves are more strongly excited than westward propagating waves in this case and the eastward and westward modes have similar magnitudes of zonal group velocity. When the boundary effects calculated from the right-hand side of (11) are removed from the momentum flux divergence, the net zonal forcing computed for the control case is less than 0.5 m s^{-1} day^{-1}, except in the sponge layer near the top where rapid damping of the westward propagating waves (Fig. 7) causes a net westward force of nearly 0.7 m s^{-1} day^{-1}. The smallness of the zonal force in the control case is evidence that, as expected for this case, gravity waves propagate through the stratospheric portion of the model domain with very little dissipation or mean-flow interaction.

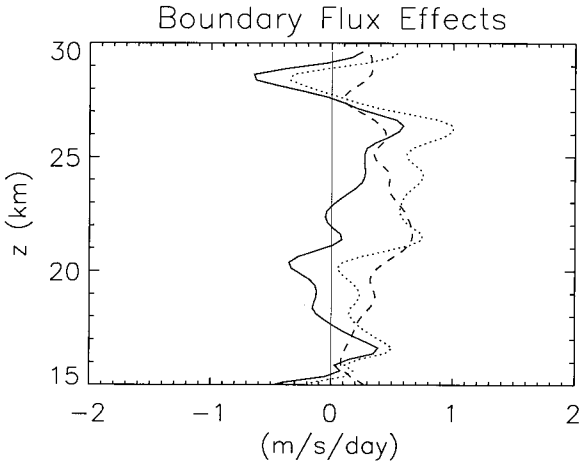

FIG. 8. The effects of wave energy fluxes leaving the side boundaries on the apparent mean-flow forcing for the control case. The dotted line shows the force per unit mass estimated directly from the convergence of the momentum flux profiles in Fig. 7. The dashed line shows the contribution due to side boundary fluxes from (11). The solid line then shows the zonal force corrected for waves leaving the domain. For this control case with no shear, the solid line gives the magnitude of unresolved errors in these calculations.

Similar zonal force calculations for the QBO easterly phase and QBO westerly phase cases (Figs. 9 and 10), on the other hand, show much different profiles of zonal forcing. In these cases the apparent forcing from waves propagating out of the domain is generally small compared to the forcing due to wave absorption in the mean-wind shear zones. As expected, a strong eastward forcing is centered in the main shear zone of the westerly QBO phase case (Fig. 10), and a strong westward forcing is centered in the main shear zone of the easterly QBO phase case (Fig. 9).

The distributions of zonal forcing shown in Figs. 9

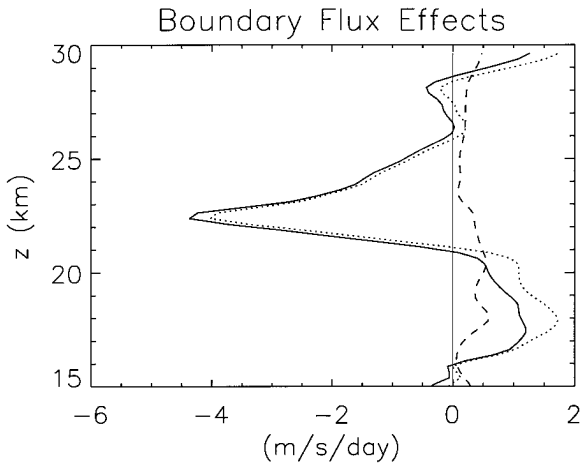

FIG. 9. Same as Fig. 8 but for the easterly shear case. Here the side boundary flux effects (dashed line) are similar to the control case, but small compared to the forcing estimated from the momentum flux convergence, which shows a strong westward peak in the easterly shear at ~22 km.

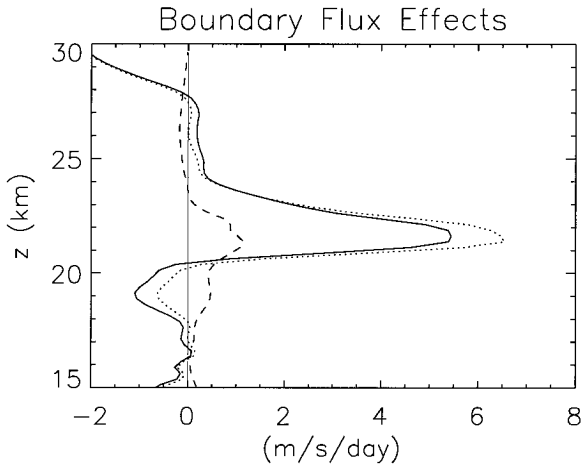

FIG. 10. Same as Fig. 8 but for the westerly shear case. As in Fig. 9, the apparent forcing associated with side boundary fluxes (dashed line) is still small but enhanced slightly in comparison to the control (Fig. 8) because of the ray bending effects of the shear. The correction reduces the magnitude of the peak eastward forcing in the westerly shear zone in this case by ~1 m s^{-1} day^{-1}.

and 10 are reminiscent of the strong forcing in shear zones characteristic of the LH68 model of the QBO. It is thus of some interest to compare the actual zonal forcing profile with that derived from the LH68 critical level absorption parameterization. According to this parameterization, the zonal forcing may be expressed as

$$-\frac{1}{\rho_s}\frac{\partial}{\partial z}(\rho_s\overline{u'w'}) = +\left|B_0(U)\exp[(z - z_0)/H]\right|\frac{dU}{dz}, \quad (12)$$

where $B_0(U) = B_0(c)$ at z_0 mapped onto the background wind field $U(z)$ and $B_0(c)$ is defined so that $\rho_0 B_0(c)dc$ is the momentum flux carried by waves in the phase speed range c to $c+dc$ evaluated at z_0, where $\rho_0 \equiv \rho_s(z_0)$. The mapping of $B_0(c)$ onto the background wind is subject to the condition that $U(z)$ must be outside the range of background wind speeds between z_0 and $z - dz$ (see Dunkerton 1996).

The flux spectra $B_0(c)$ at $z_0 = 15.875$ km for the westerly and easterly QBO phase cases are shown in Fig. 11. As expected, these are nearly identical since background flow conditions in the two simulations are identical below 16 km. The zonal force profiles resulting from mapping these spectra onto the background winds are compared with the actual zonal force profiles derived from the model fields in Fig. 12. The agreement in magnitude in the main shear zone above 20 km is good in both cases, but the parameterized forcing profile computed from (12) is shifted upward about 1–1.5 km from the actual simulated forcing profile, and the magnitude is somewhat larger, consistent with the inverse dependence on density in (12).

It is not surprising that wave damping occurs in the model as waves approach their critical levels. The dispersion relation in (6) indicates that vertical wavelength is proportional to the Doppler-shifted phase speed. As the magnitude of the Doppler-shifted phase speed decreases, damping by fourth-order diffusion becomes increasingly important. This damping can be represented as a scale-dependent Rayleigh friction and Newtonian cooling with rate coefficient $\alpha = Km^4$, where in the present case $K = 1.628 \times 10^6$ m^4 s^{-1}. The decay of momentum flux with height owing to this linear damping can be represented following HL72 (see also Dunkerton 1996) as

$$\rho_s\overline{u'w'} = \int_0^\infty \left\{ \int_{-\infty}^{+\infty} \rho_0 B_0(c, k) \cdot \exp\left[-\int_{z_0}^{z} D(c, k, z')dz' \right] dc \right\} dk. \quad (13)$$

Here

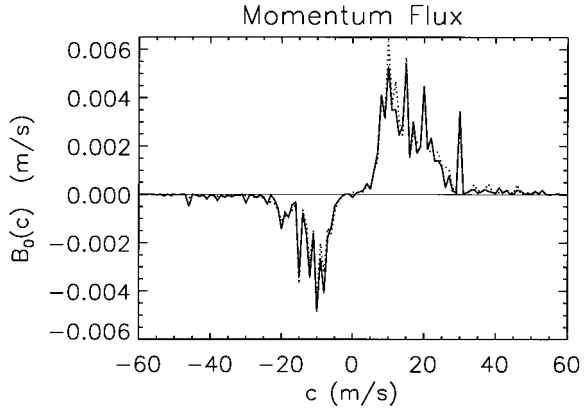

FIG. 11. Zonal intrinsic phase speed spectra of momentum flux at $z = 15.875$ km for the westerly (solid) and easterly (dotted) QBO cases.

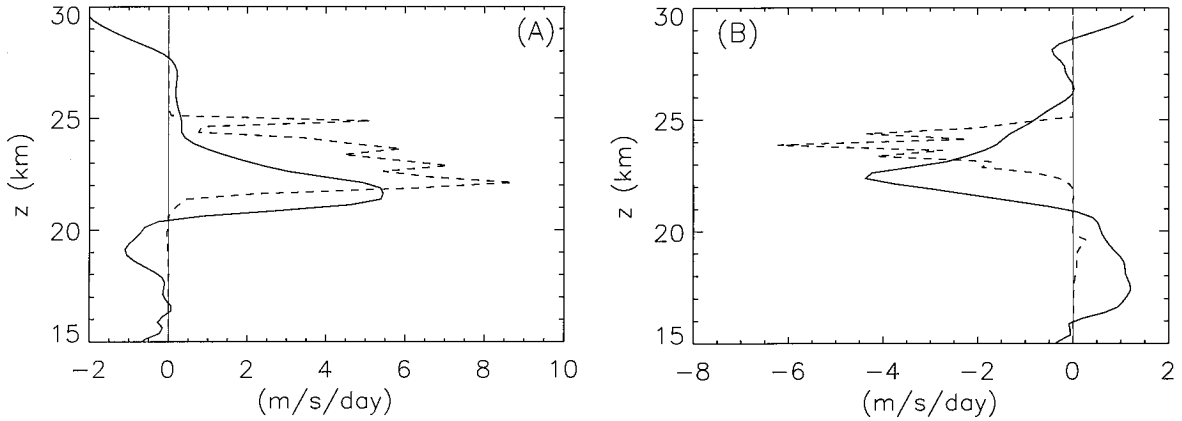

FIG. 12. Zonal force per unit mass estimated from the spectra in Fig. 11 and the LH68 model [Eq. (12)] plotted as dashed lines for (a) westerly and (b) easterly QBO cases. The boundary-flux-corrected forcing profiles from Figs. 10 and 9 are also plotted with solid lines for comparison.

$$D(c, k, z) = \frac{2Km^4N}{k(c - U)^2} \approx \frac{2KN^5}{k(c - U)^6}, \qquad (14)$$

where the far right expression holds for $m^2 \gg k^2$. It is easy to see that in this case the damping for each wave component will be strongly peaked just below the critical level as $c - U \to 0$. As shown in the appendix, an asymptotic analysis indicates that the maximum wave-induced force will then occur about 1.46 km below the critical level in the easterly shear case and 0.75 km below the critical level in the westerly shear case. The momentum flux convergence obtained from finite differencing the expression given in (13), shown in Fig. 13, provides a good approximation to the actual flux convergence of the simulated waves.

Hyperdiffusion in the model is analogous to the dissipative processes acting on gravity waves approaching critical levels in the real atmosphere. Convective and dynamical instability, and scale-selective radiative damping, are all likely to become important as the vertical wavelength decreases. Thus, as in the simulations, the zonal force produced by a given wave would be concentrated a small distance below the critical level. Linear saturation theory applied to waves with small amplitudes at their source levels would produce a similar result (e.g., Alexander and Rosenlof 1996).

The mean zonal wind acceleration, evaluated by taking the difference between a slightly smoothed version of the basic-state profile and the zonally averaged wind profile at hour 11 of the simulation divided by the time interval, is compared with the time-averaged wave-induced zonal force in Fig. 13. Although the mean wind tendencies in the main shear zones are in the same sense as the forcing for both the westerly and easterly QBO cases, the amplitude of the wind acceleration is much smaller than that of the wave-induced forcing. This failure of wave-induced forcing to be completely balanced by local flow deceleration is not surprising for a model

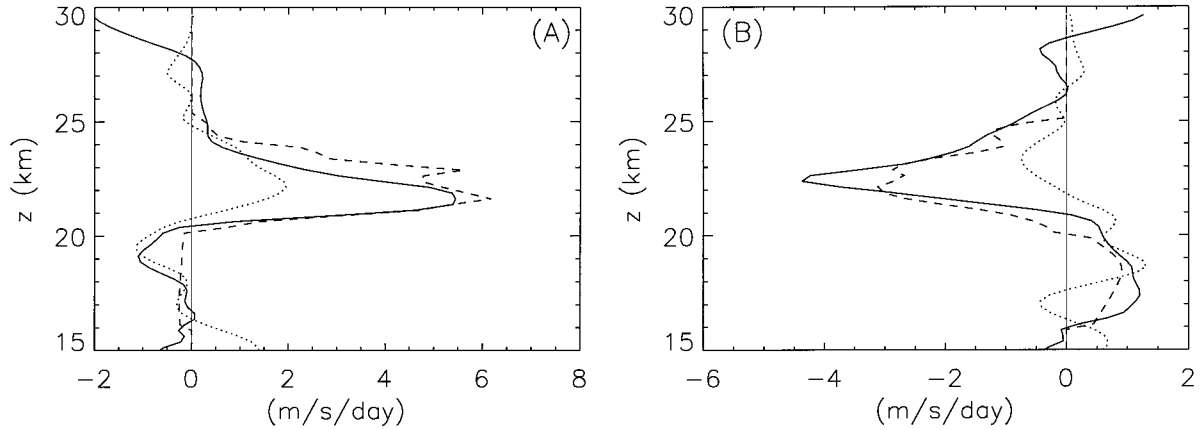

FIG. 13. Zonal force per unit mass estimated from tropopause momentum flux spectra and the dissipation model [Eq. (13); dashed lines] for the (a) westerly and (b) easterly QBO cases. These are compared to the boundary-flux-corrected profiles from Figs. 10 and 9 (solid lines). Also plotted, as dotted lines, is the change in the mean zonal wind observed in the simulations between the initial time and $t = 11$ h divided by the 11-h time interval.

with open lateral boundaries. Even though we have corrected the zonal force for the effects of gravity waves leaving the domain, there is still a net dynamic pressure gradient across the domain, which provides part of the momentum balance. As discussed by Durran (1995) in the context of mountain waves, the local wave-induced forcing generates pressure disturbances that propagate far from the forcing region and create a highly nonlocal mean flow response. The wave-induced force is thus not balanced by local accelerations, but only by the zonal flow acceleration averaged around a complete latitude circle. Hence, for evaluation of the possible impact of convectively generated gravity waves on the QBO, it is appropriate to use the computed wave-induced force, not the mean zonal wind change in the model domain.

5. Discussion: Implications for the QBO

In the observed equatorial QBO the descent rate of the westerly shear zone tends to be faster and more regular than the descent rate of the easterly shear zone. These differences are partly due to modulation of the mean upwelling rate by a secondary meridional circulation associated with the QBO and partly due to differing distributions of eastward and westward wave-induced forcing. Neglecting the asymmetries between the two phases, the average zonal acceleration rate in the QBO shear zones is of order 6 m s^{-1} $month^{-1}$, or 0.2 m s^{-1} day^{-1} (Dunkerton and Delisi 1985), averaged over the area equatorward of about $\pm 10°$ latitude. But, as noted by Dunkerton (1996), since the downward propagation of the QBO is opposed by the upwelling Brewer–Dobson circulation, a zonal force nearly twice the magnitude of the zonal wind acceleration is required to produce the observed oscillation.

The gravity wave–induced zonal forces in the westerly and easterly QBO phase squall line simulations shown in Figs. 9 and 10 are of order 5 m s^{-1} day^{-1} averaged over the model domain. If it is assumed that the length scale parallel to the simulated squall line is about 200 km, then the squall line domain is about 0.2% of the total area equatorward of $\pm 10°$ latitude. Thus, if 10 such squall lines were active on average over the entire tropical region, they could account for about 1/4 of the required zonal forcing of the QBO.

Climatological information on the areal extent of tropical convective systems has been reported by Zhang (1993) and Chen et al. (1996). According to S. Chen (1996, personal communication), the analysis of the latter paper implies that 6% of the area of the Indian Ocean and western Pacific was covered by convective systems during the intensive observation period (November 1992–February 1993) of the Tropical Ocean Global Atmosphere Coupled Ocean–Atmosphere Response Experiment (TOGA COARE). Since TOGA COARE observations were for a region and time of very active convection, the above estimate of 2% coverage for the entire equatorial area appears to be reasonable.

The West African squall line simulated in this study occurs, however, in an environment of unusually high conditional instability, so it is likely to have more intense convective cells than typical of convective storms over most of the Tropics. Also, squall lines in nature are generally not aligned strictly in the east–west direction, but at some angle, and this would further reduce the estimated zonal momentum carried by the gravity waves. Furthermore, preliminary studies with a three-dimensional version of the cloud model suggest that simulated gravity wave amplitudes are larger in the two-dimensional simulation than in three-dimensions. Thus, it is likely that mesoscale gravity waves generated by such convection actually account for somewhat less than 1/4 of the acceleration in the QBO.

Nevertheless, mesoscale gravity waves may play an important role in accounting for the observed lateral width of the equatorial QBO. LH68 focused on large-scale equatorially trapped wave modes, rather than mesoscale gravity waves, partly because such modes are trapped in the equatorial region and hence can apparently readily account for the observed decay of the QBO outside of the equatorial zone. Previous two-dimensional and three-dimensional simulations of the QBO, however, have tended to produce oscillations with meridional scales smaller than observed (e.g., Plumb and Bell 1982). Any model that depends solely on equatorial wave modes is likely to have this deficiency, since the meridional width of an equatorial mode shrinks rapidly as the wave approaches its critical level. Thus, what must be explained is not why the QBO wind oscillation is confined to the equatorial zone, but rather why the QBO is not more tightly confined to the equatorial zone than is observed.

Since vertically propagating mesoscale gravity waves will be generated wherever convection occurs, such waves should be distributed over a wide range of latitudes, rather than being confined to the equatorial zone. If such waves provide a substantial fraction of the QBO zonal forcing, it might be argued that the QBO should not be equatorially confined. P. Haynes (1994, personal communication) has shown, however, that the response to a wave-induced zonal force in the stratosphere depends strongly on the latitude where the force is applied. At low latitudes the force is balanced by a zonal wind acceleration, while at higher latitudes it is balanced by the Coriolis force of an induced meridional circulation [the extratropical pumping discussed in Holton et al. (1995)]. Consequently, even if the wave-induced forcing were distributed uniformly in latitude, the resulting zonal acceleration should be equatorially trapped. Thus, it is tempting to conclude that mesoscale gravity waves do have a significant role to play in the equatorial QBO, especially in accounting for the observed wind oscillation several degrees of latitude away from the equator.

Acknowledgments. We wish to thank Dr. Timothy Dunkerton for helpful discussions. This research was supported by the Physical Meteorology Program of the National Science Foundation under Grant ATM-9322480 and by the National Aeronautics and Space Administration under Grant NAG-1-1803.

APPENDIX

Zonal Force Induced by Diffusion

The distance below the critical level at which the maximum wave-induced force occurs for waves subject to the fourth-order vertical diffusion in the numerical model can be computed using the expressions derived in the appendix of Dunkerton (1996). From (13) the momentum flux per unit phase speed per unit wavenumber is

$$\rho_0 B(c,k,z) = \rho_0 B_0(c,k) \exp\left[-\int_{z_0}^{z} D(c,k,z')\, dz'\right], \quad \text{(A1)}$$

with $D(c, k, z)$ given by (14). Following Dunkerton the argument in the exponent in (A1) can be expressed as

$$\begin{aligned}\int_{U_0}^{U} D(c,\, k,\, U')\left(\frac{dU}{dz'}\right)^{-1} dU' &\approx \frac{2KN^5}{k\Lambda}\int_{U_0}^{U}\frac{dU'}{(c-U')^6}\\ &\approx \frac{2KN^5}{5k\Lambda(c-U)^5}, \quad \text{(A2)}\end{aligned}$$

where $\Lambda \equiv (dU/dz)_{z_c}$. Because the basic-state shear is constant in the main shear layers for both the easterly shear and westerly shear simulations, $c - U = \Lambda(z_c - z)$. Thus, (A2) can be expressed as

$$\int_{z_0}^{z} D\, dz' \approx \frac{2KN^5}{5k\Lambda^6(z_c - z)^5} \equiv \xi^5 \quad \text{(A3)}$$

and D can be expressed as

$$D = \frac{2KN^5}{k\Lambda^6(z_c - z)^6} = 5\epsilon^{-1}\xi^6, \quad \text{(A4)}$$

where $\xi \equiv \epsilon(z_c - z)^{-1}$ and $\epsilon = N[2K/(5k\Lambda^6)]^{1/5}$.

The wave-induced force per unit mass per unit phase speed per unit wavenumber is

$$\begin{aligned}A &= -\frac{1}{\rho_s}\frac{\partial}{\partial z}[\rho_0 B(c,\, k,\, z)] = \frac{\rho_0}{\rho_s} DB\\ &= \frac{5}{\epsilon} B_0 \xi^6 \exp(-\xi^5)\exp\left(\frac{z - z_0}{H}\right). \quad \text{(A5)}\end{aligned}$$

This has its maximum for $\xi \approx 1.04$. In the simulations reported here $K = 1.628\times10^6$ m^4 s^{-1} and $N = 2.2\times10^{-2}$ s^{-1}. For the westerly shear case $\Lambda = 7.0\times10^{-3}$ m^{-1} and for the easterly shear case $\Lambda = -4.0\times10^{-3}$ m^{-1}. For a zonal wavelength of 62.8 km the maximum wave-induced force thus occurs at $(z_c - z) = 1.46$ km in the easterly QBO case and $(z_c - z) = 0.75$ km in the westerly QBO case.

REFERENCES

Alexander, M. J., and L. Pfister, 1995: Gravity wave momeotum flux in the stratosphere over convection. *Geophys. Res. Lett.,* **22,** 2029–2032.

——, and K. H. Rosenlof, 1996: Non-stationary gravity wave forcing of the stratospheric zonal mean wind. *J. Geophys. Res.,* **101,** 23 465–23 474.

——, J. R. Holton, and D. R. Durran, 1995: The gravity wave response above deep convection in a squall line simulation. *J. Atmos. Sci.,* **52,** 2212–2226.

Allen, S. J., and R. A. Vincent, 1995: Gravity wave activity in the lower atmosphere: Seasonal and latitudinal variations. *J. Geophys. Res.,* **100,** 1327–1350.

Andrews, D. G., J. R. Holton, and C. B. Leovy, 1987: *Middle Atmospheric Dynamics.* Academic Press, 489 pp.

Bergman, J. W., and M. L. Salby, 1994: Equatorial wave activity derived from fluctuations in observed convection. *J. Atmos. Sci.,* **51,** 3791–3806.

Chen, S.S., R.A. Houze Jr., and B.E. Mapes, 1996: Multiscale variability of deep convection in relation to large-scale circulation in TOGA COARE. *J. Atmos. Sci.,* **53,** 1380–1409.

Dunkerton, T. J., 1991: Nonlinear propagation of zonal winds in an atmosphere with Newtonian cooling and equatorial wavedriving. *J. Atmos. Sci.,* **48,** 236–263.

——, 1996: The role of gravity waves in the quasi-biennial oscillation. *J. Geophys. Res.,* in press.

——, and D. P. Delisi, 1985: Climatology of the equatorial lower stratosphere. *J. Atmos. Sci.,* **42,** 376–396.

Durran, D. R., 1995: Do breaking mountain waves decelerate the local mean flow? *J. Atmos. Sci.,* **52,** 4010–4032.

——, and J. B. Klemp, 1983: A compressible model for the simulation of moist mountain waves. *Mon. Wea. Rev.,* **111,** 2341–2361.

Fovell, R., D. Durran, and J. R. Holton, 1992: Numerical simulations of convectively generated stratospheric gravity waves. *J. Atmos. Sci.,* **49,** 1427–1442.

Gray, L. J., and J. A. Pyle, 1989: A two-dimensional model of the quasi-biennial oscillation of ozone. *J. Atmos. Sci.,* **46,** 203–220.

Hamilton, K., and R. A. Vincent, 1995: High-resolution radiosonde data offer new prospects for research. *Eos, Trans. Amer. Geophys. Union,* **76,** 497–507.

Holton, J. R., 1972: Waves in the equatorial stratosphere generated by tropospheric heat sources. *J. Atmos. Sci.,* **29,** 368–375.

——, 1992: *Introduction to Dynamic Meteorology.* Academic Press, 511 pp.

——, and R. S. Lindzen, 1972: An updated theory for the quasi-biennial cycle of the tropical stratosphere. *J. Atmos. Sci.,* **29,** 1076–1080.

——, P. H. Haynes, M. E. McIntyre, A. R. Douglass, R. B. Rood, and L. Pfister, 1995: Stratosphere–troposphere exchange. *Rev. Geophys.,* **33,** 403–439.

Houze, R. A., Jr., 1993: *Cloud Dynamics.* Academic Press, 573 pp.

Karoly, D. J., G. L. Roff, and M. J. Reeder, 1996: Gravity wave activity associated with tropical convection detected in TOGA COARE sounding data. *Geophys. Res. Lett.,* **23,** 261–264.

Lafore, J.-P., and M. Moncrieff, 1989: A numerical investigation of the organization and interaction of the convective and stratiform regions of tropical squall lines. *J. Atmos. Sci.,* **46,** 521–544.

Lindzen, R. S., 1971: Equatorial planetary waves in shear: Part I. *J. Atmos. Sci.,* **28,** 609–622.

——, and J. R. Holton, 1968: A theory of the quasi-biennial oscillation. *J. Atmos. Sci.,* **25,** 1095–1107.

——, and C.-Y. Tsay, 1975: Wave structure of the tropical strato-

sphere over the Marshall Islands area during 1 April–1 July 1958. *J. Atmos. Sci.*, **32,** 2008–2021.

Maruyama, T., 1969: Long-term behaviour of Kelvin waves and mixed Rossby-gravity waves. *J. Meteor. Soc. Japan*, **47,** 245–254.

Pfister, L., K. R. Chan, T. P. Bui, S. Bowen, M. Legg, B. Gary, K. Kelly, M. Proffitt, and W. Starr, 1993: Gravity waves generated by a tropical cyclone during the STEP tropical field program: A case study. *J. Geophys. Res.*, **98,** 8611–8638.

Plumb, R. A., 1977: The interaction of two internal waves with the mean flow: Implications for the theory of the quasi-biennial oscillation. *J. Atmos. Sci.*, **34,** 1847–1858.

——, and R. C. Bell, 1982: A model of the quasi-biennial oscillation on an equatorial beta-plane. *Quart. J. Roy. Meteor. Soc.*, **108,** 335–352.

Redelsperger, J.-L., and J.-P. Lafore, 1988: A three-dimensional simulation of a tropical squall line: Convective organization and thermodynamic vertical transport. *J. Atmos. Sci.*, **45,** 1334–1356.

Sato, K., F. Hasegawa, and I. Hirota, 1994: Short-period disturbances in the equatorial lower stratosphere. *J. Meteor. Soc. Japan*, **72,** 859–872.

Takahashi, M., and B. A. Boville, 1992: A three-dimensional simulation of the equatorial quasi-biennial oscillation. *J. Atmos. Sci.*, **49,** 1020–1035.

Tsuda, T., Y. Murayama, H. Wiryosumarto, S. W. B. Harijono, and S. Kato, 1994: Radiosonde observations of equatorial atmosphere dynamics over Indonesia, 2, characteristics of gravity waves. *J. Geophys. Res.*, **99,** 10 507–10 516.

Wallace, J. M., and V. E. Kousky, 1968: Observational evidence of Kelvin waves in the tropical stratosphere. *J. Atmos. Sci.*, **25,** 900–907.

Zhang, C., 1993: On the annual cycle in highest, coldest clouds in the Tropics. *J. Climate*, **6,** 1987–1990.